Received: 22 December 2022 | Revised: 30 May 2023 | Accepted: 12 June 2023

DOI: 10.1002/sia.7243

RESEARCH ARTICLE

SURFACE and INTERFACE ANALYSIS WILEY

Investigating the structure of the oxide on Ni-Cr-Mo alloys while presenting a method for analysis of complex oxides using QUASES

Adam M. Morgan[1] | Jeffrey D. Henderson[2] | Brad A. Kobe[2] | Mark C. Biesinger[1,2] | James J. Noël[1,2]

[1]Department of Chemistry, Western University, London, Ontario, Canada

[2]Surface Science Western, Western University, London, Ontario, Canada

Correspondence
Mark C. Biesinger, Surface Science Western, Western University, London, Ontario, Canada.
Email: biesingr@uwo.ca

James J. Noël, Department of Chemistry, Western University, London, Ontario, Canada.
Email: jjnoel@uwo.ca

X-ray photoelectron spectroscopy (XPS) is a technique that is widely used to study thin oxide films because of its extremely high surface sensitivity. Utilizing the QUASES (Quantitative Analysis of Surfaces by Electron Spectroscopy) software package developed by Sven Tougaard (University of Southern Denmark), a user can obtain additional information that is not extracted in conventional XPS analysis, specifically the composition as a function of depth. Presented here is the QUASES analysis of four Ni-Cr-Mo alloys performed while testing various inelastic mean free path (IMFP) determination methods in the context of providing a framework for the analysis of complex oxides in QUASES. Ni-Cr-Mo alloys are often used to replace conventional materials under aggressive conditions, because of their exceptional corrosion resistance. Their corrosion resistance is conferred by the formation of an inert surface oxide film that protects the underlying metal. Using the QUASES software, the thickness of the air-formed oxide on four Ni-Cr-Mo alloys was found to lie within the range of 2.5–3.6 nm. They were found to be composed of an inner Cr_2O_3 layer and an outer $Cr(OH)_3$ layer, with a transition zone where the two coexisted. Oxidized Mo species, MoO_2 and MoO_3, were found in trace amounts at the boundary between the Cr_2O_3-only and mixed Cr_2O_3/$Cr(OH)_3$ regions of the oxide. We also determined that using 20% reduced IMFP values gave results similar to those obtained using electron effective attenuation length (EAL) values. Auger depth profiles showed comparable trends to the QUASES models.

KEYWORDS
depth profile, Hastelloy, Ni-Cr-Mo alloy, passive film, QUASES, XPS

1 | INTRODUCTION

Ni-Cr-Mo alloys exhibit excellent corrosion resistance even under aggressive conditions, including high temperatures, strong oxidants, aggressive anions, low solution pH, or some combination of these. As a result, these alloys find applications in the nuclear, pharmaceutical, chemical processing, and aerospace industries. The corrosion resistance of Ni-Cr-Mo alloys is the result of a surface oxide that is enriched in both Cr and Mo.[1] In particular, alloying additions of Cr are known to promote the formation of Cr^{III} oxides that provide excellent

protection to the underlying metal.[2,3] Alloying additions of Mo have been shown to increase film stability and promote the repair of localized damage to the film in conditions involving low solution pH.[4–6] Although the effects of alloyed Cr and Mo have been extensively studied,[3,4,7] more work is required to understand the relationship between alloy composition, oxide structure, and corrosion resistance.

Because oxide films formed on Ni-Cr-Mo alloys are typically only a few nanometers thick,[2,3,8,9] techniques with high surface sensitivity are required to study their composition and structure. The surface sensitivity (5–10 nm) of X-ray photoelectron spectroscopy (XPS) makes it an ideal technique for the study of these films.[10,11] In conventional XPS analysis, peaks in the survey and high-resolution spectra are integrated to obtain elemental and chemical state information. However, this type of analysis does not provide any structural information.

Tougaard et al. have extensively studied the energy loss processes associated with electrons in surface electron spectroscopy techniques.[12–18] They have shown that the inelastic background signal that is subtracted and discarded in conventional XPS analysis contains structural information on the nanoscale, including both depth and surface coverage information. Photoelectrons originating from deep within a surface experience an increased probability of inelastic collisions. Because of the inelastic collisions, some of the escaping photoelectrons have a lower-than-expected kinetic energy (K.E.), resulting in an increase in the background signal. On the other hand, photoelectrons originating from the outermost surface layers experience minimal inelastic collisions and consequently lose less energy. Using these principles, Tougaard developed a commercial software package called "Quantitative Analysis of Surfaces by Electron Spectroscopy" (QUASES), which analyzes the inelastic background signal associated with selected peaks in XPS spectra. Quantitative information is obtained by modeling the inelastic electron loss processes for a user-defined structure that considers both depth and surface coverage. Various surface models can be considered: a buried layer, multiple buried layers, island structures, and exponential concentration profiles. The models are deemed accurate when the simulated background and photoelectron peak contributions match the experimental spectrum.

Analyzing the inelastic background signal has been useful in studies including, but not limited to, surface oxides, nanoparticles, corrosion, and adsorption processes.[19–32] In a series of publications by Grosvenor et al., QUASES was used to study the gas-phase oxidation of pure Fe.[19,20,25–27] The authors were able to model the structure of various surface oxides and hydroxides (i.e., γ-Fe_2O_3, Fe_3O_4, FeO, FeOOH, Fe $(OH)_2$) as a function of exposure conditions, which included temperature, O_2 concentration, and exposure time. Similar studies were done by Payne et al. for oxide films formed on pure Ni after exposure to various gaseous environments.[28,29] Here, the authors were able to determine the oxidation kinetics for different atmospheric compositions (e.g., water vapor) and temperatures by using oxide thickness measurements and compositional profiles obtained from QUASES analyses. Recent work by Laszczynska et al. used QUASES to study the effect of annealing temperature on a Ni-Mo alloy coating.[30] In this study, models considering elemental species of C, O, Ni, and Mo were produced to determine the film thickness and composition at each annealing temperature. Lampimäki et al. conducted a comprehensive analysis of the oxide formed on austenitic stainless steel at various temperatures using QUASES.[31] The authors constructed a model for the FeCrNi alloy consisting of Cr_2O_3 and Fe^{II}/Fe^{III} oxides. A layer enriched in metallic nickel was also observed at the interface between the oxides and alloy. Similar work was conducted by Jussila et al. and Ali-Löytty et al. on ferritic stainless steel (Fe-17Cr).[21,32]

Previous works have focused primarily on simple systems, with analysis being conducted on one or two elements of interest to determine changes caused by an environmental factor, for example, temperature and partial pressure. Studies related to specimens with more complex surface structures have been limited, with notable work being conducted on stainless steel.[21,31,32] Here, we present a detailed procedure for the deconvolution of the air-formed oxide structures found on four commercially available Ni-Cr-Mo alloys. Improvements to one of the user-input values in QUASES, the inelastic mean free path, are discussed in the context of reducing the error associated with analyzing such complex surface structures. The selection of the other input parameter, the inelastic scattering cross-section, is also discussed. Although the experimental results are limited to air-formed oxides, the intent of this publication is to present and validate the methodology for this type of analysis. The air-formed oxide models obtained for these alloys provide a baseline for future QUASES models of Ni-Cr-Mo alloys. The approach described could also be used to extract more information from existing XPS data.

2 | EXPERIMENTAL

2.1 | Materials

2.1.1 | Hastelloy specimens

Hastelloy specimens were supplied as mill-annealed sheets by Haynes International (Kokomo, Indiana). Nominal alloy compositions provided by Haynes International are given in Table 1. The alloys were first ground using wet silicon carbide (SiC) paper from P600 to P4000 grit, then given a final polish using a 1-μm diamond suspension (Buehler MetaDi™ Monocrystalline Diamond Suspension). The specimens were then sonicated in ethanol (EtOH), rinsed with deionized (DI) water (18.2 MΩ cm), and dried in a stream of (UHP) Ar gas. All specimens were stored in a desiccator for a 72-h period prior to XPS analysis of the native oxide film. A KLA-Tencor P-17 Surface Profiler was used to obtain a roughness value for a G-30 sample that underwent surface preparation identical to that used for the XPS specimen. Three 1-mm-length line scans were conducted and then used to calculate a mean roughness average (Ra) of 3.20 nm.

TABLE 1 Nominal composition of Hastelloy family alloys, as reported by Haynes International (wt.%).

Alloy	Ni	Cr	Mo	Fe	W	Co	Mn	Si	Nb	V	Al	C	Cu
BC-1	Bal.	15	22	2	-	1^{M}	0.25^{M}	0.08^{M}	-	-	0.5^{M}	0.01^{M}	-
C-22	Bal.	22	13	3	3	2.5^{M}	0.5^{M}	0.08^{M}	-	0.35^{M}	-	0.01^{M}	0.5^{M}
G-30	Bal.	30	5.5	15	2.5	5^{M}	1.5^{M}	0.8^{M}	0.8	-	-	0.03^{M}	2
G-35	Bal.	33.2	8.1	2	0.6^{M}	1^{M}	0.5^{M}	0.6^{M}	-	-	0.4^{M}	0.05^{M}	0.3^{M}

Note: M indicates a maximum value, and Ni accounts for the balance.

2.1.2 | Reference spectra

Reference spectra were obtained for a number of pure compounds, including Cr_2O_3 (99.9%), MoO_2 (99%), MoO_3 (99.97%), and $Cr(OH)_3$. All samples were purchased from Sigma-Aldrich, with the exception of $Cr(OH)_3$, which was prepared according to the procedure described by Swaddle et al.[33] The identity and purity of all samples were confirmed using X-ray powder diffraction (XRD) and XPS. For amorphous compounds unsuited to identification by XRD analysis, Fourier transform infrared spectroscopy (FTIR) was employed. Reference spectra for metallic Cr and Mo were each obtained by sputtering through the oxide film and analyzing the bare alloy surface of a pure specimen of the respective metal.

2.2 | Surface analysis

2.2.1 | X-ray photoelectron spectroscopy

All XPS analyses were carried out on the Kratos Axis Supra spectrometer (Kratos Analytical Ltd, Manchester, UK) located at Surface Science Western. In all analyses, a take-off angle of 90° to the specimen surface was used. The instrument work function was calibrated to give a binding energy (B.E.) of 83.95 eV for the $4f_{7/2}$ signal of a metallic Au specimen. During all analyses, pressures within the analysis chamber were maintained ≤1×10^{-8} Torr. Photoelectrons were produced using a monochromatic Al K_α X-ray source (1486.6 eV) operating at 6 mA and 15 kV for the collection of survey spectra. High-resolution spectra were collected at 15 mA and 15 kV. Photoelectrons were collected from an area of 300 μm × 700 μm. Survey spectra were acquired for binding energies (B.E.) between 0 and 1200 eV using a pass energy of 160 eV and a step size of 1 eV. High-resolution spectra were acquired for the Mo 3d, Cr 2p, Ni 2p, C 1s, and O 1s regions using a pass energy of 20 eV and a step size of 0.1 eV. All spectra were charge-corrected using the aliphatic carbon signal (284.8 eV). All spectra were deconvoluted using CasaXPS (v.2.3.19). Deconvolution of high-resolution spectra was done according to the fitting parameters previously described in the literature for Ni,[34,35] Cr,[35,36] and Mo.[37,38]

2.2.2 | Auger electron spectroscopy

Auger electron spectroscopy (AES) was performed using the PHI 710 Scanning Auger Nanoprobe (Physical Instruments Inc., MN, USA) located at Surface Science Western. Survey spectra were collected from 30 to 1030 eV (K.E.) with a step size of 1 eV, over an area of 90 μm × 90 μm. To obtain depth information, specimens were sputtered with Ar^+ ions accelerated at 500 eV, over an area of 4 mm × 4 mm. Sputtering was performed for 1.2 s, followed by data acquisition. This cycle was repeated until a total sputter time of 120 s was reached. For the oxide films formed on the Hastelloy specimens, sputter rates and times were converted into approximate resultant sputter depths using the experimentally measured sputter rate of a Si wafer containing a 100-nm-thick SiO_2 overlayer. Under the same conditions used for the Hastelloy specimens, the sputter rate of SiO_2 was ~2 nm min^{-1}. Peaks selected for analysis during the depth profiling were determined from the original AES survey spectra.

2.3 | Inelastic background signal analysis

The inelastic background signal was analyzed using the "Quantitative Analysis of Surfaces by Electron Spectroscopy" (QUASES) software package (v. 5.4) developed by Sven Tougaard.[39] The principles behind QUASES analyses were developed by Tougaard et al. and have been extensively described in the literature.[12,15,17,40–42] Values of the inelastic mean free path (IMFP) for pure species were calculated according to the TPP-2M equation of Tanuma, Powel, and Penn.[43] Values of electron effective attenuation length (EAL) were calculated using the NIST Electron Effective-Attenuation-Length Database (v. 1.3).[44] The asymmetry parameters necessary in the EAL calculations were provided by Yeh et al.[45,46] The QUASES-Generate program, which analyzes spectra by calculating the background of inelastically scattered electrons expected from a theoretical model specimen and comparing such model spectra to a measured spectrum, was utilized for all instances in this study.

3 | RESULTS AND DISCUSSION

3.1 | Method development

Similar to conventional high-resolution XPS analyses, QUASES-Generate analyses of experimental signals are conducted using reference spectra obtained from pure metal and oxide specimens. For example, consider the Cr 2p spectral region signal obtained for alloy BC-1, Figure 1, which overlays reference spectra of Cr in three chemical states: the metal (metallic Cr), oxide (Cr_2O_3), and hydroxide

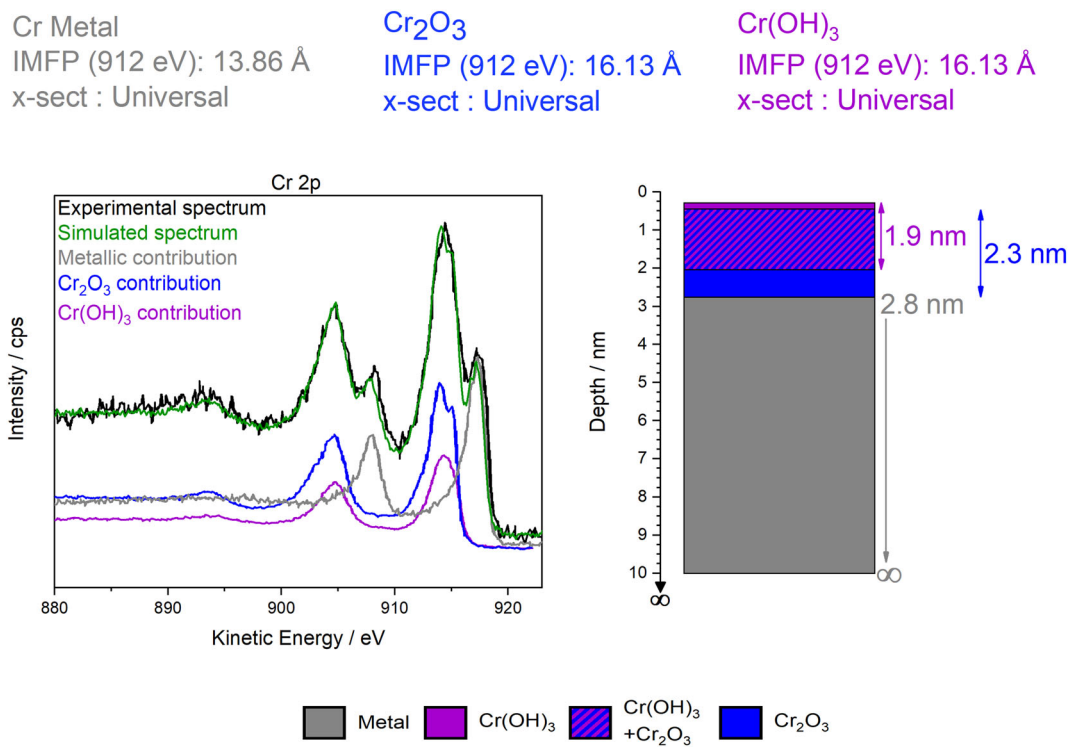

FIGURE 1 QUASES analysis of the Cr 2p peak for alloy BC-1. The contributions of both oxidized and metallic reference spectra to the simulated spectrum are shown, along with the resulting surface model produced by the simulation. The inelastic mean free path values (20% reduced weighted average IMFPs) and the cross-section (x-sect) utilized are displayed.

($Cr(OH)_3$). The peaks in the BC-1 spectrum can be deconvoluted on the basis of the peaks found in the reference spectra to provide speciation of the specimen surface. The inelastic background signal in the BC-1 spectrum contains some information about the depth of buried Cr atoms/ions that can be extracted by QUASES. This extraction is based on the inelastic background signal of the input reference spectra. These principles also apply to the deconvolution of the Mo 3d peak, which was accomplished using reference spectra of metallic Mo, MoO_2, and MoO_3 (Figure 2). The QUASES deconvolution of the Cr 2p and Mo 3d peaks for all models presented in this study are provided in the Supporting Information (Figures S1–S12). Prior to QUASES deconvolution, all reference spectra were processed according to the procedure recommended in the software manual.[47] This included a correction for the energy dependence of the analyzer transmission and a subtraction of the initial background signal. Only corrected reference spectra were considered in the deconvolution of experimental spectra.

The experimental data were fitted by generating a simulated spectrum that contained peak contributions and background signals from each of the reference spectra. Adequate fits were obtained when the simulated spectrum closely matched the experimental spectrum, including the background signal. Because the simulated background signals are directly related to the structure of the adjustable surface models in QUASES, quantifiable information can be obtained. For the deconvoluted Cr 2p and Mo 3d peaks shown in Figures 1 and 2, respectively, a simulated spectrum was found to match the experimental data when a series of buried layers were considered. The location and thickness of each buried layer will be discussed in more detail below.

The structural information obtained from the separate analyses of the Cr 2p and Mo 3d peaks was combined into a final model that considers the position of the metal and both Cr and Mo oxides, shown in Figure 3. In this final model, the outermost surface layer represents adventitious carbon and other adsorbed species. When the models for Mo and Cr were combined, we retained the starting depth of the metal determined by analysis of the Cr 2p peak in the final model, as analysis of this peak produced a model that contains the interface between metal and oxide. The starting depth for the metal obtained by analysis of the Cr 2p and Mo 3d peaks was identical for both BC-1 (22 wt.% Mo) and C-22 (13 wt.% Mo), which are the higher-Mo-content alloys. For G-35 (8.1 wt.% Mo) and G-30 (5.5 wt.% Mo), there was a 0.2 nm and a 1.2 nm difference in the determined metal starting depth, respectively. This difference can likely be attributed to the additional error associated with analyzing spectra of less-abundant elements, as the difference increases when the Mo content of the alloy decreases.

While simulating the inelastic background signal for each of the reference spectra, several input parameters are required, including the selection of an inelastic scattering cross-section and values for the IMFP. Here, these two parameters are discussed in the context of minimizing error. The first input parameter required for the simulation of an inelastic background with QUASES is the inelastic scattering

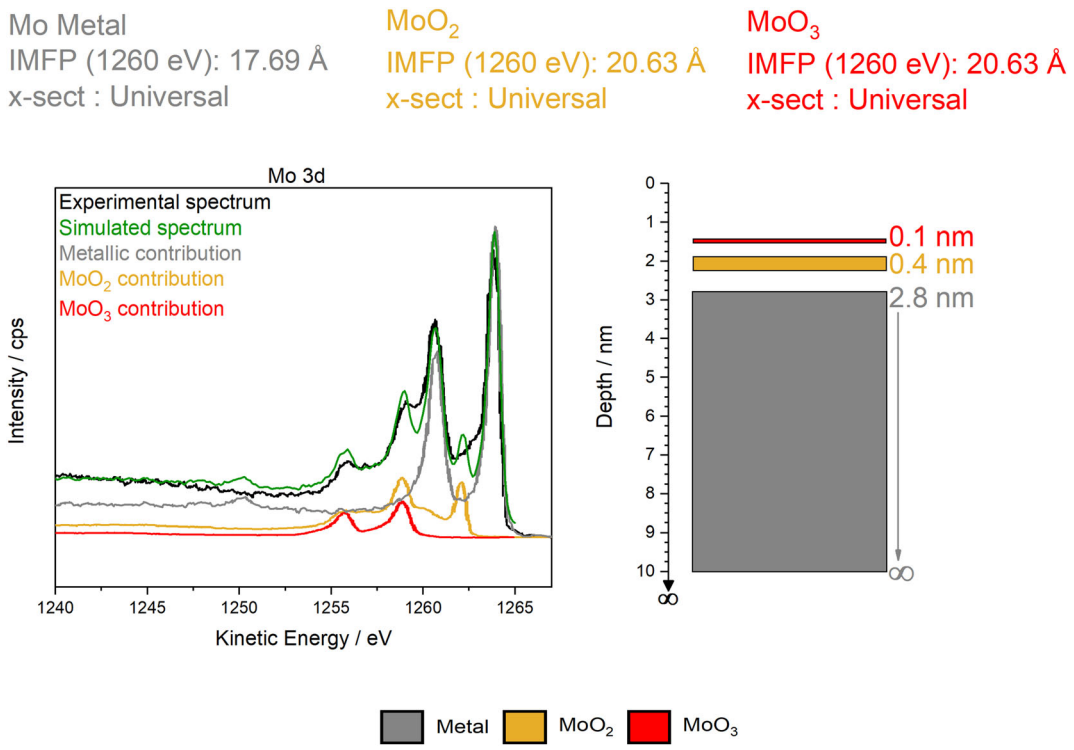

FIGURE 2 QUASES analysis of the Mo 3d peak for alloy BC-1. The contributions of both oxidized and metallic reference spectra to the simulated spectrum are shown, along with the resulting surface model produced by the simulation. The inelastic mean free path values (20% reduced weighted average IMFPs) and the cross-section (x-sect) utilized are displayed.

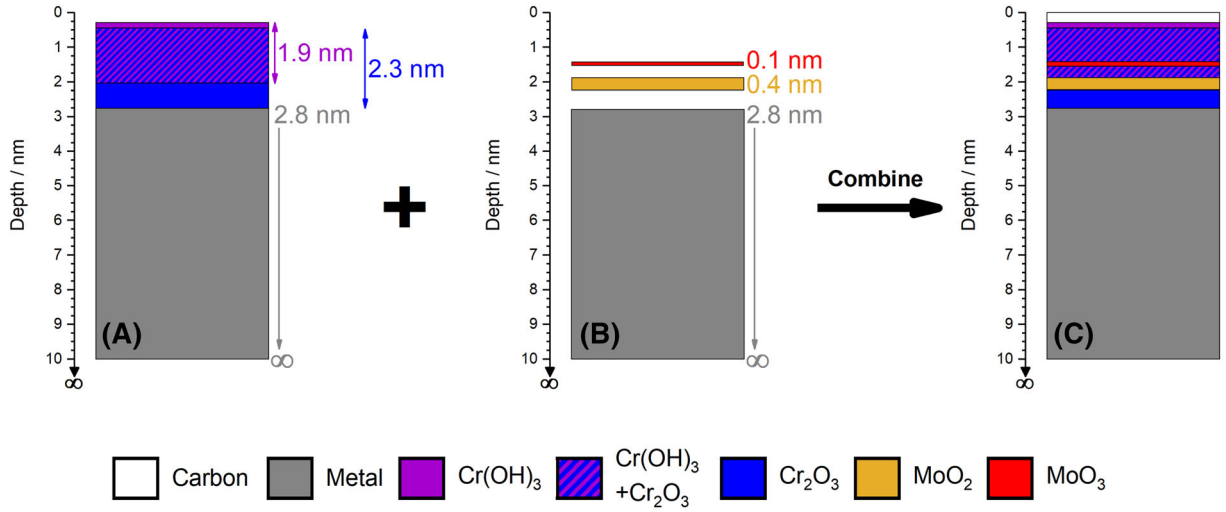

FIGURE 3 Results obtained using the QUASES software for the air-formed oxide present on alloy BC-1. Models obtained via analysis of the Cr 2p (A) and Mo 3d (B) spectra are combined into a final model shown in (C).

cross-section. The inelastic scattering cross-section describes the change in energy distribution of electrons traveling in a solid and therefore affects the shape of the background signal, and the IMFP describes the intensity of the background signal. For the example used in this paper, the universal cross-section was utilized in all instances for the analysis of Cr and Mo peaks. The universal cross-section has been proven to describe the cross-section for most metals and their respective oxides with sufficient accuracy[41] and has been utilized in many studies.[19,22,48,49] For other solids (i.e., Al, Si, SiO_2, Ge, and polymers), an alternative cross-section is required to describe the electron energy loss processes accurately. Using the reflected electron energy-loss spectroscopy (REELS) method of cross-section determination, Tougaard demonstrated that the cross-section for Si has a distinct plasmon peak at 16.8 eV.[41] This feature of a distinct plasmon

structure is seen in the cross-section of other free-electron-like solids, such as Al, Si, SiO_2, and Ge, and therefore, a unique cross-section is required for each of these solids. In contrast, it was found that Fe has a significantly broader cross-section, because of a more complex band structure, in which multiple groups of electrons contribute to the electron energy loss process.[41] Similar to Fe, most metals and their oxides display a broad cross-section profile where the width of the prominent shape in the cross-section is greater than ~15–20 eV, and therefore, the universal cross-section was developed. As previously mentioned, the universal cross-section was utilized in all instances in this study; however, certain challenges are presented when performing inelastic background signal analysis of samples that contain elements that have different inelastic scattering cross-sections. In this respect, significant advancements to this user input value have been made to overcome this difficulty and obtain more accurate elemental depth distributions.[50–52] Risterucci et al. analyzed an Al/Ti bilayer structure in an AlGaN/GaN power transistor device stack using hard X-ray photoelectron spectroscopy (HAXPES). In this case, the background signal of the photoelectron peaks had contributions from the universal cross-section (due to metallic Ti), an aluminum cross-section, and, in some cases, a TiO_2 cross-section. They were able to obtain improved background signal analysis by using an effective cross-section, calculated as the weighted sum of the individual cross-sections of each layer. The extent to which these cross-sections were blended was guided by the nominal composition from high-resolution core-level analysis. Effective cross-sections have also been used to increase the accuracy of inelastic background signal analysis with HAXPES of Al/Ta bilayers[51] and theoretical bilayer structures consisting of combinations of Al, Si, polymer, Ta, and Au.[52] The ability to blend cross-sections has been implemented in Ver 6.0 of the QUASES-Tougaard software.[39]

The second input parameter required is an IMFP value. Because the IMFP is a material-dependent value describing the average distance that a photoelectron can travel between inelastic collisions, it should reflect the specific environment in which the photoelectron is traveling. Commonly in QUASES analyses, the IMFP values utilized are from the dominant metal species and the dominant oxide species, when modeling the metal and oxides, respectively. Previous studies, which focused on simple systems, have used this straightforward approach for determining IMFP values. For example, in the study of an oxidized Ni specimen, Payne et al. deconvoluted and modeled the Ni 2p peak using reference spectra obtained for Ni metal and NiO.[29] During the simulation of inelastic background signals, IMFP values for either Ni metal or NiO were used, depending on the reference spectra (i.e., $(IMFP)_{Ni}$ for Ni and $(IMFP)_{NiO}$ for NiO). In the case of Ni-Cr-Mo alloys, Ni is the dominant metal species (from the nominal composition) and Cr_2O_3 is commonly considered to be the dominant oxide species. For illustrative purposes, we conducted such a QUASES analysis on the XPS signals from a Hastelloy BC-1 specimen, using the IMFP of Cr_2O_3 for electrons emitted from atoms in the air-formed oxide layer and the IMFP of Ni metal for electrons originating in the metal substrate. The best-fit model output is shown in Figure 4A.

However, it is easy to understand that the use of the dominant species IMFP values introduces some errors, because the oxide is not simply made of Cr_2O_3, nor is the alloy made of pure Ni. Moreover, photoelectrons emitted from the metal would have to pass through the oxide and experience its IMFP before they could reach the detector. This is problematic; for example, the IMFP for a photoelectron (K.E. [Cr 2p] = ~912 eV) traveling through metallic Cr is less than its IMFP in Cr_2O_3 (16.10 and 18.33 Å, respectively). Furthermore, this difference in IMFP increases as photoelectrons become more energetic. For instance, consider the Mo 3d signal, which has photoelectrons exiting the specimen with a kinetic energy of ~1260 eV. The calculated IMFP values for metallic Mo and MoO_3 are 19.80 and 24.00 Å, respectively. This is further complicated for multielement systems (e.g., stainless steel) where the IMFP of individual elements should be considered and weighted appropriately. In some previous works, authors have reported utilizing an IMFP value in QUASES that has been averaged between Cr and Fe oxides in the analyses of stainless steel.[21,31,32] More recently, an effective IMFP (based on weighted averaging) has been utilized in inelastic background signal analysis.[50–52] Risterucci et al. used a weighted average IMFP based on the nominal thickness of each layer in the analysis of an Al/Ti bilayer structure in an AlGaN/GaN power transistor device stack. Zborowski et al. analyzed Al/Ta/AlGaN stacks on a GaN substrate, and as previously mentioned, they blended the cross-sections of Al and Ta to varying degrees to create an effective cross-section.[51] Additionally, an effective IMFP value with weighting factors corresponding to the blending between Al and Ta (e.g., 50:50 and 60:40) was utilized in the background signal analysis.[51] Zborowski et al. also conducted a theoretical study of bilayer systems consisting of different combinations of Al, Si, polymer, Ta, and Au.[52] In this study, they used two different IMFP determination methods. The first was a weighted average based on the thickness of the surface and buried layer. For the second method, they reasoned that in a bilayer system, the photoelectrons that are emitted from the buried layer will not all be emitted from the deepest point and that on average, the electrons will come from the middle of the buried layer. Therefore, only half of the thickness of the buried layer and the full thickness of the surface layer were considered in this effective IMFP calculation. They found the latter approach gave them better fits for most bilayer combinations when compared with an effective IMFP that considered both the surface and buried layer equally.

These approaches often use knowledge of layer thicknesses in their determination of the IMFP value; however, in many applications, the layer thicknesses and order are unknown and are often the goal of conducting inelastic background signal analysis. Moreover, the proponents of such approaches did not consider the experimentally determined surface composition in formulating their IMFP values, leaving room for improvement in QUASES analyses. The concept of a weighted average IMFP value based on high-resolution analysis is not novel. Biesinger et al. utilized a weighted average IMFP based on experimentally determined surface compositions when calculating the film thickness of Ni[34] and Cu[53] samples. The film thickness was

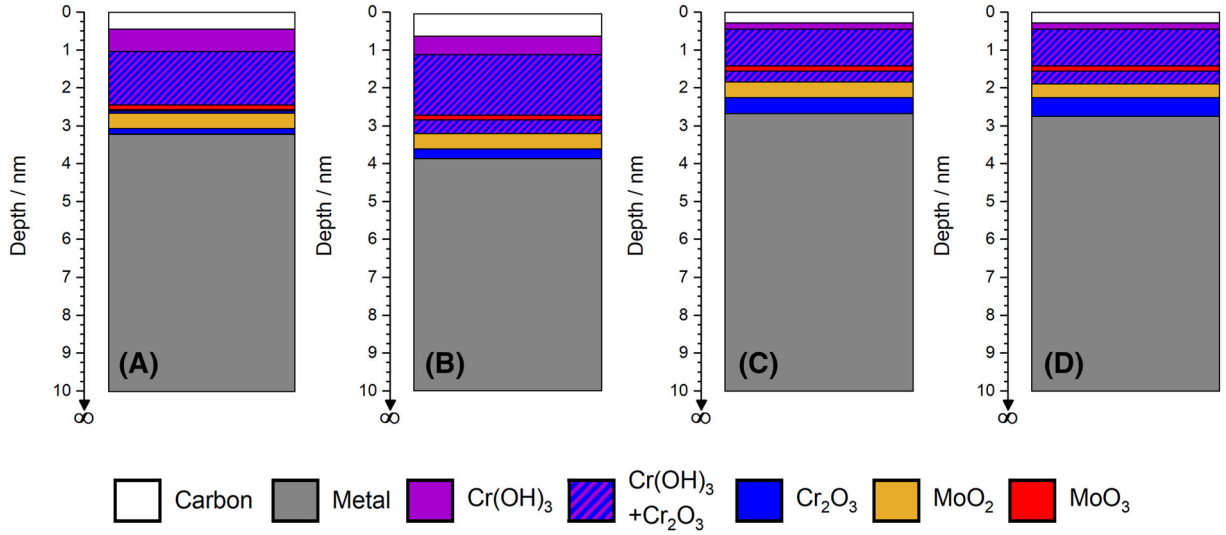

FIGURE 4 Surface models for the air-formed oxide on Hastelloy alloy BC-1 using (A) a dominant species IMFP, (B) a weighted average IMFP, (C) a weighted average EAL, (D) and a 20% reduced weighted average IMFP.

obtained through calculations of the type used by Carlson[54] and Strohmeier[55]; however, this type of analysis gives no information on how these oxides/hydroxides are distributed throughout the film. Although the IMFP is a source of inherent error, improvements to the way the IMFP value is calculated can help reduce the magnitude of this error by determining IMFP values that reflect the realities discussed above. Here, a method is presented for the determination of IMFP values that more accurately represent the environment experienced by the escaping photoelectron in the analysis of complex films consisting of mixed oxidized species.

In this improved representation, two scenarios exist for escaping photoelectrons: They originate from within the oxide layer and are subject to its IMFP, which we denote as $IMFP_1$, or they originate from within the metal and pass through the oxide layer ($IMFP_2$), initially experiencing the IMFP of the metallic alloy, followed by $IMFP_1$ as they escape the specimen through the oxide. We estimated the $IMFP_1$ and $IMFP_2$ values as follows. In the first case, photoelectrons produced in the oxide layer should experience a weighted average IMFP that could be calculated using the experimentally determined composition of only the oxide layer, that is, $IMFP_1$. This weighted average can be calculated according to Equation (1),

$$IMFP_1 = \sum_i (IMFP_i)(X_i) \quad (1)$$

where $IMFP_i$ is the calculated IMFP value for each metal oxide or hydroxide species, i, and X_i indicates the mole fraction of that same (hydr)oxide species among all the oxidized species present in the film. A shortcoming of this approach, however, is that it treats the oxide as if it is completely homogeneous.

In the second case, for photoelectrons produced from atoms within the metallic layer buried beneath the surface oxide film, an IMFP value that accounts for both metallic and oxidized species in the escape path should be considered. This weighted average can be calculated according to Equation (2),

$$IMFP_2 = \sum_j (IMFP_j)(X_j) \quad (2)$$

where $IMFP_j$ is the calculated IMFP value for each species, j, for which an XPS signal was measured (in both oxide film and underlying metal) and X_j indicates the relative abundance of each species based on the deconvolution of the measured signal for all species detected (in both oxide film and underlying metal, Figure 5C). The resulting model obtained using a weighted average IMFP in QUASES is shown in Figure 4B.

Surface concentrations (i.e., X_i and X_j) were obtained experimentally using the survey and high-resolution XPS spectra. An example of this is shown for alloy BC-1 in Figure 5. First, the general surface composition was quantified from the survey spectrum and analyzed in the conventional way (Figure 5A). To calculate the IMFP, only the ratios of the major alloying elements were considered, that is, Ni, Cr, and Mo. The adventitious carbon signal was omitted from the IMFP calculation because it was present in only small amounts and has a significantly larger IMFP than do the other elements considered. For the elements quantified in the survey spectrum, corresponding high-resolution spectra were deconvoluted using fitting parameters readily available in the literature, to obtain chemical state information.[34–38] For example, consider the deconvoluted Cr $2p_{3/2}$ band shown in Figure 5B. Three species were present: metallic Cr, Cr_2O_3, and Cr $(OH)_3$. Combining the information from the survey and high-resolution spectra, the chemical composition of the surface was determined and used to calculate a more realistic IMFP value. According to Figure 5A,B, the surface of BC-1 contained 26 at.% Cr, and of that amount, 36% was in the metallic state, 46% was present as Cr $(OH)_3$, and 18% was present as Cr_2O_3. A representation showing the

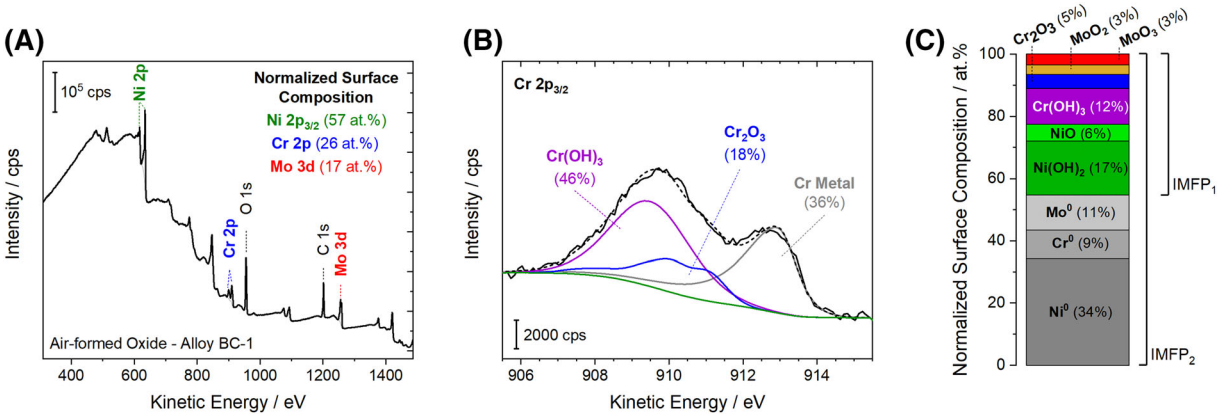

FIGURE 5 XPS fitting of Hastelloy BC-1. (A) Quantified survey and (B) deconvoluted high-resolution Cr 2p3/2 spectra are displayed. Atomic and chemical information from analysis of the survey and high-resolution scans, respectively, were used to create the (C) normalized surface composition representation.

normalized surface composition is given in Figure 5C. Here, the metallic and oxidized components are grouped separately, because the latter are assumed to form on the outermost portion of this surface; however, beyond this, no other structural information is assumed or obtained from conventional analysis of the survey and high-resolution spectra, and this representation is not intended to depict a specific layer structure or any layers at all, save for the oxide layer and the substrate metal (and note that knowledge of even these layers does not come from conventional XPS). The normalized surface compositions of all alloys analyzed in this study can be found in the Supporting Information (Figure S13).

We also investigated the consequences of using electron EAL values in place of IMFP values within the software. This approach originates from Grosvenor's analysis of oxides on Fe specimens; in his work, the model calculated by QUASES had a significantly larger oxide thickness (~20%) than that determined by nuclear reaction analysis (NRA).[19] Grosvenor attributed this to using the IMFP rather than the electron EAL in QUASES modeling. The IMFP is a calculated value that only considers the effect of inelastic collisions, whereas the EAL considers both inelastic and elastic collisions on the transit of electrons through a material.[56,57] Therefore, an EAL value was determined for all nine species that were considered in the weighted IMFP calculation, at each of the two peak energies (Cr 2p and Mo 3d), for a total of 18 EAL values. The EAL values were calculated using the NIST Electron Effective-Attenuation-Length Database.[44] This calculation requires the IMFP and the transport mean free path (TMFP), both of which are calculated by the NIST software. The database also requires the photoionization asymmetry parameter; these data were provided by Yeh et al.[45,46] This produces an EAL for a given overlayer thickness. The EAL was selected at an overlayer thickness of 3.0 nm, as this was the average oxide thickness value determined by QUASES analysis for these alloys. However, it is important to note that the EAL values in the range of 2.5–3.6 nm for a given species did not differ by more than 0.2 Å. The EAL for Cr_2O_3 at 912 eV was calculated to be 14.56 Å, signifying a ~21% reduction from the determined IMFP value of 18.33 Å. Across all 18 IMFP and EAL values, the EAL was on average 21% lower than the IMFP, indicating excellent agreement with Grosvenor's empirically proposed 20% IMFP reduction. The EAL value for each species was weighted according to the determined surface compositions (i.e., IMFP is replaced with EAL in Equations 1 and 2) to produce a weighted average EAL. The model determined in this fashion for alloy BC-1 is displayed in Figure 4C. When we used a weighted average EAL value in the model, the film thickness decreased compared with the result obtained using a weighted average IMFP value, whereas the overall oxide layer structure remained consistent.

To determine whether the simple 20% IMFP reduction proposed by Grosvenor is an accurate reflection of the difference between using EAL and IMFP values (i.e., it quickly yields acceptable layer thickness without requiring a calculation involving EAL, TMFP, and photoionization asymmetry parameter values), we conducted a comparison that included all species in our system, using a weighted average IMFP with an applied 20% reduction. The resulting model obtained from QUASES is shown in Figure 4D. The weighted IMFP values for both metal and oxide layers were reduced by a factor of 20% (Equations 3 and 4).

$$IMFP_1 = \sum_i (IMFP_i)(X_i) \times 0.8 \quad (3)$$

$$IMFP_2 = \sum_j (IMFP_j)(X_j) \times 0.8 \quad (4)$$

Comparing Figure 4B and 4D, the 20% reduction in IMFP values caused the amount of each oxide film component to decrease and the total thickness of the oxide film to decrease from 3.2 nm (Figure 4B) to 2.5 nm (Figure 4D). This approximate 20% reduction in film thickness is expected when using a 20% IMFP reduction.

Figure 4 illustrates the influence of the IMFP parameter on QUASES model results for each of the approaches to determining a value to use for the IMFP, using Hastelloy BC-1 as a case for comparison. Summarizing the results, the overall layer structure and order

remained constant, but slight changes to the layer thicknesses were observed. Figure 4A shows the QUASES model produced when we used the IMFP value of Cr_2O_3 for photoelectrons derived from all oxide and hydroxide species and that of Ni for photoelectrons derived from all metallic species. As discussed previously, an improvement to the typical approach may be achieved by using a weighted average IMFP, as presented in Figure 4B. Comparing Figure 4A and 4B, an increase in the overall layer thickness was obtained when the weighted average IMFP was used because the IMFP used for both the metal and oxide components increased in the weighted model. The IMFP for the "metal" layer increased because of the consideration of both metal and oxide/hydroxide components, which typically have higher IMFPs than do pure metals, in this combined parameter; the IMFP for the oxide/hydroxide layer increased because of the consideration of the multiple oxidized species that are present in addition to Cr_2O_3, particularly the hydroxide species (i.e., Cr $(OH)_3$ and Ni $(OH)_2$), which have especially high IMFP values.

Further improvements can be made by using either a weighted average EAL or a 20% reduced weighted average IMFP, both of which produced nearly identical models. For BC-1, the only difference between these two methods was a 0.1 nm shift in the metal-Cr_2O_3 interface (Figure 4C,D); similar observations were seen for the other three alloys. It is possible to use the EAL in place of the IMFP in QUASES, however, that requires a pre-determined estimate for overlayer thickness, which is often the main output parameter from the QUASES analysis, rather than an available input figure. Additionally, the use of a weighted average IMFP with a 20% reduction was shown to produce results that were nearly identical to those derived using a weighted average EAL. Therefore, the use of a weighted average IMFP value with a 20% reduction is a simple but valid way to provide increased agreement with oxide thickness measurements determined by other techniques. For example, the Auger depth profiles, shown in Figure 6, indicated that the oxide thickness for the four alloys ranged from ~1 to 2 nm. Additionally, Henderson et al. found that the air-formed oxide on BC-1 is 1–2 nm thick, using XPS and time-of-flight secondary ion mass spectrometry (ToF-SIMS),[9] whereas Lloyd et al. found that the air-formed oxide on alloy C-22 is 1.8 nm using ToF-SIMS profiles.[8] For these reasons, this was the IMFP determination method used for the remaining three Ni-Cr-Mo alloys (Figure 7). Despite using a 20% reduction to the IMFP value, we found that the oxide thickness values for Ni-Cr-Mo alloys that we determined using QUASES (2.5–3.6 nm), shown in Figure 7, were consistently larger than oxide thickness values determined by other techniques. This leaves room for future investigations on determining an IMFP value that will give more accurate values for film thickness in a complex system.

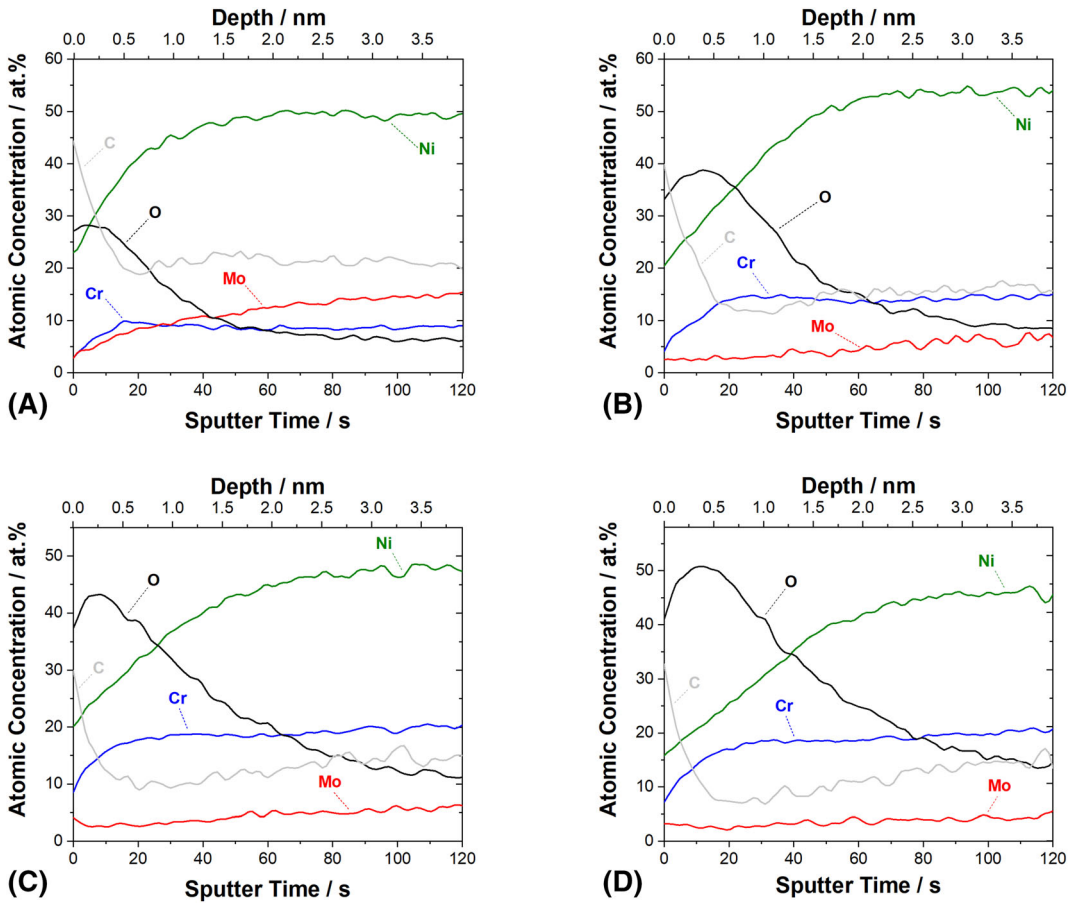

FIGURE 6 Auger depth profiles obtained for the Hastelloy alloys (A) BC-1, (B) C-22, (C) G-35, and (D) G-30.

3.2 | Ni-Cr-Mo alloys: air-formed oxide

Simulated models for the air-formed oxides grown on all four Hastelloy alloys are displayed in Figure 7 using a 20% reduced weighted average IMFP. Comparing the models to each other, we see that the air-formed oxide present on each alloy was dominated by an oxidized Cr layer and that these layers are on the scale of a few nanometers. Additionally, the oxide thickness was found to increase with an increasing amount of alloyed Cr, though slight disagreement in this trend was exhibited between G-35 (33 wt.% Cr) and G-30 (30 wt.% Cr), which had 3.3- and 3.6-nm-thick oxide films, respectively. Though this difference between G-35 and G-30 is very likely to be within the range of experimental error, Auger depth profiles, found in Figure 6, exhibited the same trend as the QUASES models. Also, the effect of differing amounts of alloyed Fe (G-35 [2 wt.% Fe] and G-30 [15 wt.% Fe]) on oxide thickness is a likely cause, but we have not yet confirmed this. Furthermore, for all alloys, the Cr oxide layer was found to have a Cr $(OH)_3$-dominated outer portion, a Cr_2O_3-dominated inner portion, and a region containing both Cr species. Auger depth profiles were conducted with the purpose of confirming our QUASES results and are displayed in Figure 6. Many challenges are present when using sputtering techniques for the analysis of nanometer scale oxide films, such as the difference in sputter rates between the calibration material and the metal oxide of the sample. Therefore, the depth profiles were analyzed only for general trends rather than absolute values. From the Auger depth profiles, a trend of increasing oxide thickness as a function of increasing Cr content was observed. Additionally, the same trends were observed when we compared the oxide depth profiles obtained by Auger electron spectroscopy with the QUASES simulated models: The oxide thickness trends were identical (G-30 > G-35 > C-22 > BC-1), and the thickness generally increased with increasing amounts of alloyed Cr; they are on the scale of a few nanometers, and minimal amounts of Mo are present in the oxide.

We compared the results obtained from QUASES with those from previous analyses of the native oxides on Ni-Cr-Mo alloys, found in the literature. The overall thickness of the air-formed oxide was on the scale of a few nm, which is expected for Ni-Cr-Mo alloys.[2,3,8,9] It is known that the oxide on Ni-Cr-Mo alloys is dominated by Cr species and that the film thickness increases with the amount of alloyed Cr.[2,3] Zhang et al. showed the same oxide profile for the Ni-Cr-Mo alloy C-2000: Cr $(OH)_3$ concentrated in the outer portion, Cr_2O_3 concentrated in the inner portion, and a region with both species present.[10,58] The presence of hydroxide on the outer portion was expected, as the hydroxide layer originates from the hydrolysis of cations that have been ejected from the inner Cr_2O_3 layer.[10] Unsurprisingly, on all the alloys investigated, the amount of Mo in the oxide was minimal, but it was found to be higher for the high-Mo alloys, BC-1 (22 wt.% Mo), and C-22 (13 wt.% Mo). Overall, the results of the models in QUASES would be expected to change under different exposure conditions and may represent a direction of future work. For example, it has been shown that Cr and Mo have dynamic behavior during transpassive dissolution.[59]

The QUASES models shown in Figure 7 provide important information on the nanoscale; however, they are not an entirely realistic model of the passive film structure. Figure 8 displays the QUASES model for BC-1 (Figure 8A) with an added illustration to consider some of these realities (Figure 8B). For example, there will be some effect of roughness at the metal-film, film-carbon, and carbon-atmosphere interfaces. The portion of the QUASES model where there is an overlap between Cr $(OH)_3$ and Cr_2O_3 (purple and blue stripes) will likely comprise a concentration gradient of these two oxidized species. In the outer portion of the overlap region, there will

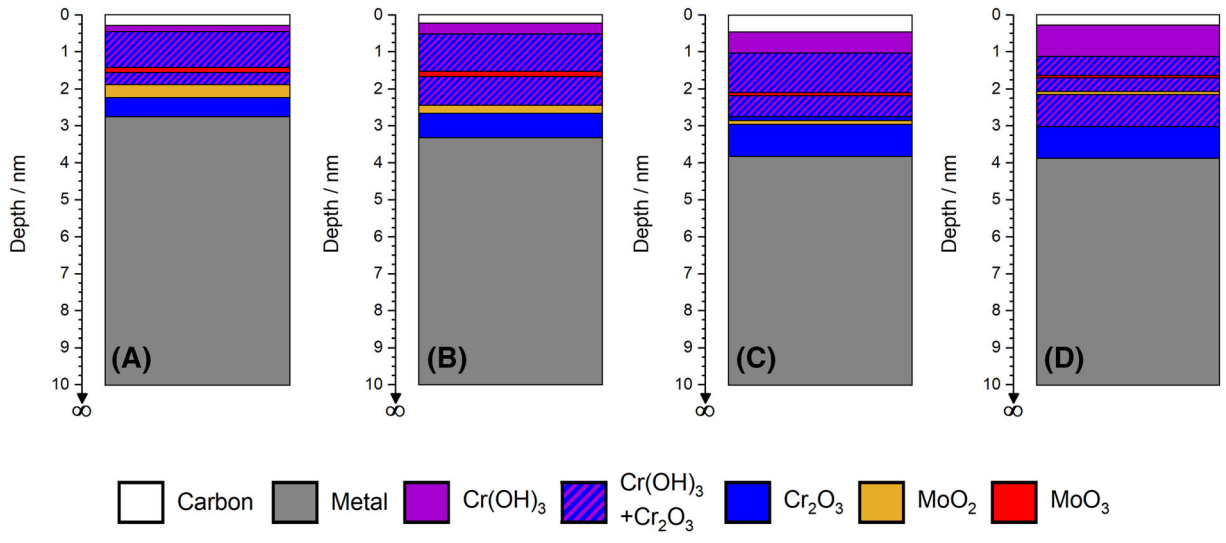

FIGURE 7 Air-formed oxide models for the Hastelloy alloys (A) BC-1, (B) C-22, (C) G-35, and (D) G-30 obtained using the QUASES software. Experimental spectra were simulated using reference spectra from pure standards to produce each model. A 20% reduced weighted average IMFP was utilized in the modeling.

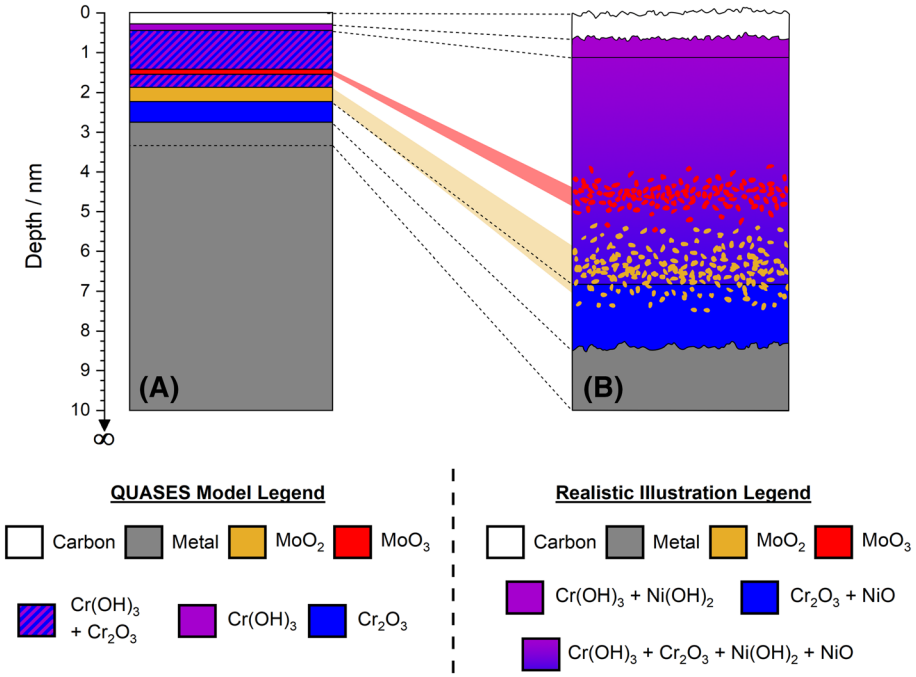

FIGURE 8 (A) Air-formed oxide model of BC-1 determined by QUASES using 20% reduced weighted average IMFPs and (B) a realistic illustration of the surface structure of alloy BC-1.

likely be a higher amount of Cr $(OH)_3$ relative to Cr_2O_3, rather than the 50:50 split that the QUASES model suggests. The same can be said for the inner portion of the overlap region, where there is likely a higher amount of Cr_2O_3 relative to Cr $(OH)_3$. The presence of a concentration gradient between Cr $(OH)_3$ and Cr_2O_3 is supported by ToF-SIMS cross-sectional images of Ni-Cr-Mo alloy C-2000.[10,58] For molybdenum, the QUASES models show that the oxides are present as extremely thin and discrete layers, which is not an accurate representation of Mo within the film. Typical Mo–O bond distances are approximately 0.2 nm,[60,61] whereas the thickness of the molybdenum oxide layers determined from QUASES can be as low as 0.04 nm for some alloys (i.e., G-30 and G-35). Therefore, the MoO_2 and MoO_3 layers in the QUASES models should be viewed in the context of their average position within the film. In reality, the Mo oxides likely do not form a discrete layer but rather are localized in small clusters (shown as small red and orange circles in Figure 8) and are mixed with other film components. Various studies are in agreement with this hypothesis.[62,63] Yu et al. conducted atom probe tomography on a thermally grown film on a Ni-22Cr-6Mo alloy and found that oxidized molybdenum species appear in small clusters rather than forming a discrete layer within the film.[62] Using a nonequilibrium solute capture framework, it was theorized that individual Mo cations are incorporated into the growing Ni (II) and Cr (III) oxide films.[62] In a separate study, Massoud et al. used electrochemical scanning tunneling microscopy and found that oxides grown on Fe-18Cr-13Ni alloys exhibited nanoscale depressions in the passive film.[64] However, Maurice et al. later determined using scanning tunneling microscopy that these depressions were partially or completely filled for the film on a Fe-17Cr-14.5Ni-2.3Mo alloy, indicating a localized and healing role for Mo within the passive film.[63] Finally, the consideration of Ni oxides and hydroxides would need to be included to provide a more complete model for the oxide film of a Ni-Cr-Mo alloy. Therefore, the probable location of NiO and Ni $(OH)_2$ was included in this illustration to provide the most realistic interpretation of the QUASES model. In this graphic, Ni hydroxide and oxide are found at depths similar to those at which we find Cr hydroxide and Cr oxide, respectively. There is substantial evidence in the literature that suggest Ni $(OH)_2$ will coexist with Cr $(OH)_3$ and that NiO will coexist with Cr_2O_3. Zhang et al. used angle-resolved XPS to investigate the film on Alloy C-2000 and found that signals from Ni and Cr hydroxides increased, whereas those from Ni and Cr oxides decreased when a smaller take-off angle was used.[10] Additionally, ToF-SIMS cross-sectional images showed a correlation between Ni and Cr oxides and hydroxides.[10,58] Furthermore, Yu et al. observed using APT that oxidized Cr and Ni species coexist throughout the depth of the film while Mo was found in small clusters.

4 | CONCLUSIONS

Here, a method for the analysis of specimens with complex surface compositions using QUASES has been presented. The QUASES software enabled us to measure overlayer thickness while deconvoluting the contributions of individual oxidation states of atoms in a specimen with a mixed oxide. Within the software, various methods of IMFP determination were tested and discussed. These included the common procedure that uses the IMFP of the dominant oxide and metal, a weighted average IMFP, a weighted average EAL, and a 20% reduced weighted average IMFP. The use of each of these four techniques produced models with identical layer ordering/structure. This indicates that the software is fairly robust to changes in IMFP value; however, we showed that small tweaks to the IMFP value can

produce varying film thickness values. Using a weighted average IMFP minimizes the error associated with the IMFP value by considering all species present in a complex oxide mixture. Grosvenor's 20% reduction in the IMFP value was also tested.[19] It was found that this reduction causes film thickness values determined by QUASES to decrease, leading to better agreement between the QUASES model and other methods of film thickness determination. It gave results that were very similar to those obtained by using EAL values in place of IMFP values, but without requiring extra calculations based on IMFP, TMFP, and photoionization asymmetry parameter values, so, although not a rigorous treatment, it was much easier to implement. Therefore, a 20% reduced weighted average IMFP value was utilized for modeling the air-formed oxides of alloys BC-1, C-22, G35, and G-30.

Additionally, the investigation of complex surface structures in QUASES can be easily simplified by this IMFP determination method. The analysis of air-formed oxides present on Hastelloy alloys determined that the oxide thickness was within the range of 2.5–3.6 nm, and the film was composed of an inner Cr_2O_3 layer and an outer $Cr(OH)_3$ layer. There was also a transition zone where the two coexisted that likely represents a concentration gradient of the two species. Oxidized Mo species, MoO_2 and MoO_3, were found in trace amounts within the Cr-rich oxide layer. It is probable that the Mo layers in the QUASES model represent the average position of Mo oxide clusters within the film, rather than a discrete layer. A trend of increasing oxide thickness with increasing Cr content was found in both the QUASES and Auger depth profile analysis.

ACKNOWLEDGMENTS

All materials used in this study were supplied by Haynes International. The authors would like to acknowledge Dr. Sven Tougaard for the development of the QUASES software. Author A.M. would also like to thank the staff at Surface Science Western for their assistance, specifically Dr. Sridhar Ramamurthy for his help with AES depth profiling and Dr. Heng-Yong for assistance with the profilometry measurements. The authors also thank Mr. Giles Whitaker (Giles Whitaker Design) for his assistance with the illustration presented in Figure 8.

DATA AVAILABILITY STATEMENT

The data that supports the findings of this study are available in the supplementary material of this article.

ORCID

Adam M. Morgan https://orcid.org/0000-0002-7290-2594
Brad A. Kobe https://orcid.org/0000-0002-6708-7687
Mark C. Biesinger https://orcid.org/0000-0002-5714-4668

REFERENCES

1. Hayes JR, Gray JJ, Szmodis AW, Orme CA. Influence of chromium and molybdenum on the corrosion of nickel-based alloys. *Corros Sci*. 2006;62(6):491-500. doi:10.5006/1.3279907
2. Lloyd AC, Noël JJ, Mcintyre NS, Shoesmith DW. The open-circuit ennoblement of alloy C-22 and other Ni-Cr-Mo alloys. *J Miner Met Mater Soc*. 2005;57(1):31-35. doi:10.1007/s11837-005-0061-x
3. Lloyd AC, Noël JJ, Mcintyre S, Shoesmith DW. Cr, Mo and W alloying additions in Ni and their effect on passivity. *Electrochim Acta*. 2004;49(17-18):3015-3027. doi:10.1016/j.electacta.2004.01.061
4. Ebrahimi N, Jakupi P, Noël JJ, Shoesmith DW. The role of alloying elements on the crevice corrosion behavior of Ni-Cr-Mo alloys. *Corrosion*. 2015;71(12):1441-1451. doi:10.5006/1848
5. Jakupi P, Wang F, Noël JJ, Shoesmith DW. Corrosion product analysis on crevice corroded Alloy-22 specimens. *Corros Sci*. 2011;53(5):1670-1679. doi:10.1016/j.corsci.2011.01.028
6. Henderson JD, Ebrahimi N, Dehnavi V, Guo M, Shoesmith DW, Noël JJ. The role of internal cathodic support during the crevice corrosion of Ni-Cr-Mo alloys. *Electrochim Acta*. 2018;283:1600-1608. doi:10.1016/j.electacta.2018.07.048
7. Rockel B, The M. Effect of molybdenum on the corrosion behavior of iron-chromium alloys. *Corrosion*. 1973;29(10):393-396. doi:10.5006/0010-9312-29.10.393
8. Lloyd AC, Shoesmith DW, McIntyre NS, Noël JJ. Effects of temperature and potential on the passive corrosion properties of alloys C22 and C276. *J Electrochem Soc*. 2003;150(4):B120. doi:10.1149/1.1554914
9. Henderson JD, Seyeux A, Zanna S, et al. Investigating the transport mechanisms governing the oxidation of Hastelloy BC-1 by in situ ToF-SIMS. *Corros Sci*. 2019;159:108138. doi:10.1016/j.corsci.2019.108138
10. Zhang X, Zagidulin D, Shoesmith DW. Characterization of film properties on the NiCrMo alloy C-2000. *Electrochim Acta*. 2013;89:814-822. doi:10.1016/j.electacta.2012.11.029
11. Kobe B, Badley M, Henderson JD, Anderson S, Biesinger MC, Shoesmith D. Application of quantitative X-ray photoelectron spectroscopy (XPS) imaging: investigation of Ni-Cr-Mo alloys exposed to crevice corrosion solution. *Surf Interface Anal*. 2017;49(13):1345-1350. doi:10.1002/sia.6325
12. Tougaard S. Quantitative analysis of the inelastic background in surface electron spectroscopy. *Surf Interface Anal*. 1988;11(9):453-472. doi:10.1002/sia.740110902
13. Tougaard S. Practical algorithm for background subtraction. *Surf Sci*. 1989;216(3):343-360. doi:10.1016/0039-6028(89)90380-4
14. Tougaard S, Hansen HS. Non-destructive depth profiling through quantitative analysis of surface electron spectra. *Surf Interface Anal*. 1989;14(11):730-738. doi:10.1002/sia.740141109
15. Tougaard S. Inelastic background correction and quantitative surface analysis. *J Electron Spectros Relat Phenomena*. 1990;52(C):243-271. doi:10.1016/0368-2048(90)85022-2
16. Tougaard S. Surface nanostructure determination by x-ray photoemission spectroscopy peak shape analysis. *J Vac Sci Technol a Vacuum, Surfaces, Film*. 1996;14(3):1415-1423. doi:10.1116/1.579963
17. Tougaard S. Accuracy of the non-destructive surface nanostructure quantification technique based on analysis of the XPS or AES peak shape. *Surf Interface Anal*. 1998;26(4):249-269. doi:10.1002/(SICI)1096-9918(199804)26:43.0.CO;2-A
18. Tougaard S. Energy loss in XPS: fundamental processes and applications for quantification, non-destructive depth profiling and 3D imaging. *J Electron Spectros Relat Phenomena* Published online. 2010;178-179:128-153. doi:10.1016/j.elspec.2009.08.005
19. Grosvenor AP, Kobe BA, McIntyre NS, Tougaard S, Lennard WN. Use of QUASES™/XPS measurements to determine the oxide composition and thickness on an iron substrate. *Surf Interface Anal*. 2004;36(7):632-639. doi:10.1002/sia.1842
20. Grosvenor AP, Kobe BA, McIntyre NS. Examination of the oxidation of iron by oxygen using X-ray photoelectron spectroscopy and QUASES™. *Surf Sci*. 2004;565(2–3):151-162. doi:10.1016/j.susc.2004.06.210
21. Ali-Löytty H, Jussila P, Hirsimäki M, Valden M. Influence of CrN surface compound on the initial stages of high temperature oxidation of

ferritic stainless steel. *Appl Surf Sci*. 2011;257(17):7783-7791. doi:10.1016/j.apsusc.2011.04.029

22. Lesiak B, Zemek J, Jiricek P, Malolepszy A, Stobinski L. Influence of the preparation conditions of Pd-ZrO2 and AuPd-ZrO2 nanoparticle–decorated functionalised MWCNTs: electron spectroscopy study aided with the QUASES. *Surf Interface Anal*. 2017;49(11):1124-1134. doi:10.1002/sia.6290
23. Lesiak B, Jiricek P, Bieloshapka I. Chemical and structural properties of Pd nanoparticle-decorated graphene—electron spectroscopic methods and QUASES. *Appl Surf Sci*. 2017;404:300-309. doi:10.1016/j.apsusc.2017.01.183
24. Lesiak B, Mierzwa B, Jiricek P, Bieloshapka I, Juchniewicz K, Borodzinski A. Effect of treatment at high temperatures on morphology of a carbon supported Pd catalyst investigated by X-ray diffraction and photoelectron spectroscopy aided with QUASES. *Appl Surf Sci*. 2018;458:855-863. doi:10.1016/j.apsusc.2018.07.137
25. Grosvenor AP, Kobe BA, McIntyre NS. Studies of the oxidation of iron by air after being exposed to water vapour using angle-resolved x-ray photoelectron spectroscopy and QUASES ™. *Surf Interface Anal*. 2004;36(13):1637-1641. doi:10.1002/sia.1992
26. Grosvenor AP, Kobe BA, McIntyre NS. Studies of the oxidation of iron by water vapour using X-ray photoelectron spectroscopy and QUASES™. *Surf Sci*. 2004;572(2–3):217-227. doi:10.1016/j.susc.2004.08.035
27. Grosvenor AP, Kobe BA, McIntyre NS. Activation energies for the oxidation of iron by oxygen gas and water vapour. *Surf Sci*. 2005;574(2–3):317-321. doi:10.1016/j.susc.2004.10.043
28. Payne BP, Grosvenor AP, Biesinger MC, Kobe BA, McIntyre NS. Structure and growth of oxides on polycrystalline nickel surfaces. *Surf Interface Anal*. 2007;39(7):582-592. doi:10.1002/sia.2565
29. Payne BP, Biesinger MC, McIntyre NS. The study of polycrystalline nickel metal oxidation by water vapour. *J Electron Spectros Relat Phenomena*. 2009;175(1–3):55-65. doi:10.1016/j.elspec.2009.07.006
30. Laszczyńska A, Tylus W, Szczygieł B, Szczygieł I. Influence of post−deposition heat treatment on the properties of electrodeposited Ni−Mo alloy coatings. *Appl Surf Sci*. 2018;462:432-443. doi:10.1016/j.apsusc.2018.08.160
31. Lampimäki M, Lahtonen K, Jussila P, Hirsimäki M, Valden M. Morphology and composition of nanoscale surface oxides on Fe–20Cr–18Ni{111} austenitic stainless steel. *J Electron Spectros Relat Phenomena*. 2007;154(3):69-78. doi:10.1016/j.elspec.2006.12.002
32. Jussila P, Ali-Löytty H, Lahtonen K, Hirsimäki M, Valden M. Inhibition of initial surface oxidation by strongly bound hydroxyl species and Cr segregation: H2O and O2 adsorption on Fe–17Cr. *Surf Sci*. 2009;603(19):3005-3010. doi:10.1016/j.susc.2009.08.006
33. Swaddle TW, Lipton JH, Guastalla G, Bayliss P. The aqueous chemistry of chromium(III) above 100 °C: hydrothermal synthesis of chromium Spinels. *Can J Chem*. 1971;49(14):2433-2441. doi:10.1139/v71-397
34. Biesinger MC, Payne BP, Lau LWM, Gerson A, Smart RSC. X-ray photoelectron spectroscopic chemical state quantification of mixed nickel metal, oxide and hydroxide systems. *Surf Interface Anal*. 2009;41(4):324-332. doi:10.1002/sia.3026
35. Biesinger MC, Payne BP, Grosvenor AP, Lau LWM, Gerson AR, Smart RSC. Resolving surface chemical states in XPS analysis of first row transition metals, oxides and hydroxides: Cr, Mn, Fe, Co and Ni. *Appl Surf Sci*. 2011;257(7):2717-2730. doi:10.1016/j.apsusc.2010.10.051
36. Biesinger MC, Brown C, Mycroft JR, Davidson RD, McIntyre NS. X-ray photoelectron spectroscopy studies of chromium compounds. *Surf Interface Anal*. 2004;36(12):1550-1563. doi:10.1002/sia.1983
37. Spevack PA, McIntyre NS. Thermal reduction of MoO3. *J Phys Chem*. 1992;96(22):9029-9035. doi:10.1021/j100201a062
38. De Vito E, Marcus P. XPS study of passive films formed on molybdenum-implanted austenitic stainless steels. *Surf Interface Anal*. 1992;19(1–12):403-408. doi:10.1002/sia.740190175
39. Tougaard S. *Software Packages to Characterize Surface Nano-Structures by Analysis of Electron Spectra*. http://www.quases.com
40. Tougaard S, Sigmund P. Influence of elastic and inelastic scattering on energy spectra of electrons emitted from solids. *Phys Rev B*. 1982;25(7):4452-4466. doi:10.1103/PhysRevB.25.4452
41. Tougaard S. Universality classes of inelastic electron scattering cross-sections. *Surf Interface Anal*. 1997;25(3):137-154. doi:10.1002/(SICI)1096-9918(199703)25:33.0.CO;2-L
42. Graat P, Somers MAJ. Quantitative analysis of overlapping XPS peaks by spectrum reconstruction: determination of the thickness and composition of thin iron oxide films. *Surf Interface Anal*. 1998;26(11):773-782. doi:10.1002/(SICI)1096-9918(199810)26:113.0.CO;2-#
43. Tanuma S, Powell CJ, Penn DR. Calculations of electron inelastic mean free paths for 31 materials. *Surf Interface Anal*. 1988;11(11):577-589. doi:10.1002/sia.740111107
44. Powell CJ, Jablonski A. *NIST Electron Effective-Attenuation-Length Database - Version 1.3*. National Institute of Standards and Technology; 2011.
45. Yeh JJ, Lindau I. Atomic subshell photoionization cross sections and asymmetry parameters: 1 ≤ Z ≤ 103. *At Data Nucl Data Tables*. 1985;32(1):1-155. doi:10.1016/0092-640X(85)90016-6
46. Yeh JJ. *Atomic Calculation of Photoionization Cross-Sections and Asymmetry Parameters*. Gordon and Breach Science Publishers; 1993.
47. Tougaard S. *QUASES-Tougaard User's Guide Version 5.4*.; 2014.
48. Schleberger M, Fujita D, Tougaard S. Characteristic depth of the excitation function for Auger electrons in the noble metals Cu, Ag and Au determined by inelastic background analysis. *J Electron Spectros Relat Phenomena*. 1996;82(3):173-178. doi:10.1016/S0368-2048(96)03064-2
49. Yubero F, Jansson C, Batchelor DR, Tougaard S. Validity of the method for quantitative XPS of surface nano-structures: application to Cu/Au/Cu. *Surf Sci*. 1995;331-333(PART A):753-758. doi:10.1016/0039-6028(95)00275-8
50. Risterucci P, Renault O, Zborowski C, et al. Effective inelastic scattering cross-sections for background analysis in HAXPES of deeply buried layers. *Appl Surf Sci*. 2017;402:78-85. doi:10.1016/j.apsusc.2017.01.046
51. Zborowski C, Renault O, Torres A, Yamashita Y, Grenet G, Tougaard S. Determination of the input parameters for inelastic background analysis combined with HAXPES using a reference sample. *Appl Surf Sci*. 2018;432:60-70. doi:10.1016/j.apsusc.2017.06.081
52. Zborowski C, Tougaard S. Theoretical study toward rationalizing inelastic background analysis of buried layers in XPS and HAXPES. *Surf Interface Anal*. 2019;51(8):857-873. doi:10.1002/sia.6660
53. Biesinger MC. Advanced analysis of copper X-ray photoelectron spectra. *Surf Interface Anal*. 2017;49(13):1325-1334. doi:10.1002/sia.6239
54. Carlson TA, McGuire GE. Study of the X-ray photoelectron spectrum of tungsten-tungsten oxide as a function of thickness of the surface oxide layer. *J Electron Spectros Relat Phenomena*. 1972;1(2):161-168. doi:10.1016/0368-2048(72)80029-X
55. Strohmeier BR. An ESCA method for determining the oxide thickness on aluminum alloys. *Surf Interface Anal*. 1990;15(1):51-56. doi:10.1002/sia.740150109
56. Chent YF, Kweitg CM, Tung CJ. Electron inelastic mean free paths versus attenuation lengths in solids. *J Phys D Appl Phys*. 1992;25(2):262-268. doi:10.1088/0022-3727/25/2/020
57. Jablonski A, Powell CJ. The electron attenuation length revisited. *Surf Sci Rep*. 2002;47(2–3):33-91. doi:10.1016/S0167-5729(02)00031-6
58. Zhang X, Shoesmith DW. Influence of temperature on passive film properties on Ni-Cr-Mo alloy C-2000. *Corros Sci*. 2013;76:424-431. doi:10.1016/j.corsci.2013.07.016

59. Henderson JD, Li X, Shoesmith DW, Noël JJ, Ogle K. Molybdenum surface enrichment and release during transpassive dissolution of Ni-based alloys. *Corros Sci*. 2019;147:32-40. doi:10.1016/j.corsci.2018.11.005
60. Brandt BG, Skapski AC. A refinement of the crystal structure of molybdenum dioxide. *Acta Chem Scand*. 1967;21(3):661-672. doi:10.3891/acta.chem.scand.21-0661
61. McCarron EM, Calabrese JC. The growth and single crystal structure of a high pressure phase of molybdenum trioxide: MoO3-II. *J Solid State Chem*. 1991;91(1):121-125. doi:10.1016/0022-4596(91)90064-O
62. Yu XX, Gulec A, Sherman Q, et al. Nonequilibrium solute capture in passivating oxide films. *Phys Rev Lett*. 2018;121(14):145701. doi:10.1103/PhysRevLett.121.145701
63. Maurice V, Peng H, Klein LH, Seyeux A, Zanna S, Marcus P. Effects of molybdenum on the composition and nanoscale morphology of passivated austenitic stainless steel surfaces. *Faraday Discuss*. 2015;180(0):151-170. doi:10.1039/C4FD00231H
64. Massoud T, Maurice V, Klein LH, Marcus P. Nanoscale morphology and atomic structure of passive films on stainless steel. *J Electrochem Soc*. 2013;160(6):C232-C238. doi:10.1149/2.067306jes

SUPPORTING INFORMATION

Additional supporting information can be found online in the Supporting Information section at the end of this article.

How to cite this article: Morgan AM, Henderson JD, Kobe BA, Biesinger MC, Noël JJ. Investigating the structure of the oxide on Ni-Cr-Mo alloys while presenting a method for analysis of complex oxides using QUASES. *Surf Interface Anal*. 2023;55(10):749-762. doi:10.1002/sia.7243